Influence of Bowen Ratio on Boundary-Layer Cloud Structure

D. C. LEWELLEN AND W. S. LEWELLEN

West Virginia University, Morgantown, West Virginia

S. YOH

Kean College of New Jersey, Union, New Jersey

(Manuscript received 4 November 1994, in final form 9 August 1995)

ABSTRACT

An investigation of the influence of the ratio of surface sensible heat flux to latent heat flux, the Bowen ratio, on the structure of boundary-layer clouds is carried out utilizing numerical large eddy simulations (LES). The role of cloud-top radiational cooling, cloud-top temperature and moisture jump conditions, and wind shear are included in a secondary way. Although no detailed comparisons have been made, the LES results appear to be qualitatively consistent with the Atlantic Stratocumulus Transition Experiment, the recent field study on marine boundary-layer cloud structure. Some conclusions that follow from an examination of these LES results are the following: First, there is a highly bimodal character to the cloud ceiling frequency within a very low Bowen ratio boundary layer. The updrafts tend to produce a lower cloud ceiling than the surrounding environment with its weak downdrafts. Second, a very low Bowen ratio with the aid of some boundary-layer shear makes the development of persistent microcell cloud circulations possible within the boundary layer. Third, when the surface latent heat flux is the dominant factor in the dynamics of the boundary layer, the approach to a conditionally stable lapse rate results in the potential for subsequent decoupling. Last, the maximum partial cloud fraction is very well represented by the relation suggested by Sommeria and Deardorff for a Gaussian probability distribution for the range of conditions studied.

1. Introduction

Even a casual weather observer cannot help but be impressed with the myriad of low-level cloud structures. A better understanding and modeling capability of this variety is important for a number of reasons. First, these clouds have a direct impact on visibility and the operation of aircraft, and other visibility sensitive missions. Second, they play a critical role in the earth's energy balance and, thus, must be modeled accurately for any valid simulation of global weather modification. Third, the clouds interact strongly with atmospheric chemistry of various trace gases. Finally, active clouds can have a strong influence on the dynamics of the boundary layer and thus can be important to the accuracy of any regional forecast. A review of low-level cloud structures may be found in Cotton and Anthes (1989) and Emanuel (1994).

In this study, we have used large eddy simulations (LES) to investigate the sensitivity of boundary layer cloud structures to a number of physical variables. Particular attention has been placed on the influence of the Bowen ratio, the ratio of surface sensible heat flux to latent heat flux. The role of cloud-top radiational cooling, cloud-top temperature and moisture jump conditions, wind shear, and relative boundary-layer thickness are included in a secondary way. Moeng and Sullivan (1994) have looked at the differences between shear-driven and buoyancy-driven boundary layers. Moeng et al. (1992) have also studied the effect of radiational cloud-top cooling in a stratus-topped boundary layer. They restricted themselves to conditions without significant cloud-top entrainment instability (CTEI) and to essentially stationary boundary conditions. Under these conditions the fluxes of heat and moisture are linear in height. They show that the net flux profiles may be partitioned into component process fluxes, with each of these also being essentially linear in height.

We restrict our attention to boundary layers where the turbulence is dominated by buoyancy. This buoyancy may be generated from surface heating, either sensible or latent, or by cooling near the top of the boundary layer, either via radiation or cloud-top evaporation. We examine the differences these modes of turbulent generation can have on the cloud structure. We also look at the role a modest amount of shear may have in organizing the cloud structure.

Corresponding author address: Dr. W. S. Lewellen, Mechanical and Aerospace Engineering, West Virginia University, P.O. Box 6106, Morgantown, WV 26506-6106.
E-mail: wsl@wvnvms.wvnet.edu

We are interested in determining cloud structure features such as the partial cloud fraction, the rate of cloud-top entrainment, and the large-scale cloud organization. We demonstrate that, for our selection of runs, the partial cloud fraction is well represented by the Sommeria and Deardorff (1977) relation. The rate of entrainment correlates with the Richardson number based on the characteristic vertical velocity in the cloud layer, a measure of cloud-top thickness, and the virtual potential temperature jump across the capping inversion. One of the results coming out of the Atlantic Stratocumulus Transition Experiment (ASTEX) field study is that under some circumstances the boundary layer turbulence can become quite organized, and an individual cloud representing the top of a single recirculating cell, or cluster of cells, can persist for more than an hour. Our results show that such a persistent cloud is possible when the turbulence is dominated by buoyancy generated from latent heat release, if a moderate amount of wind shear is added to the boundary layer. The wind shear appears to dampen relatively weak circulations and favor the clustering of the stronger cells.

2. LES model review

The basic LES model used is that described by Sykes and Henn (1989) with the cloud dynamics as given by Sykes et al. (1990). The subgrid closure utilizes a quasi-equilibrium, second-order turbulence closure scheme with the maximum turbulence length scale related to the numerical grid length. The model includes the possibility for partial cloudiness within an individual grid cell to allow us to deal with small-scale mixing between cloudy and clear air. The subgrid cloudiness parameterization is that given for Gaussian probability distribution functions (Sommeria and Deardorff 1977; Mellor 1977). This formulation has the degree of cloud fraction in an individual grid cell depending upon the ratio of the mean saturation level to the square root of the local saturation variance. We carry the saturation variance as an additional prognostic variable consistent with our second-order closure scheme. The expectation is that the dominant updrafts and downdrafts are sufficiently resolved that the binormal probability distribution function model of partial cloudiness given by Lewellen and Yoh (1993) is not needed. A number of simulations at different ambient conditions were used, with uniform horizontal grids over domains of from 3 to 12 km. Approximately 60 vertical grid points were used with variable spacing down to a minimum of 10 m in the vicinity of the inversion and 5 m at the surface. Sensitivity to both the domain size and the grid resolution are discussed in the appendix.

New features added to the code are the incorporation of the piecewise parabolic model of advection for humidity and temperature (Sykes et al. 1994) and the addition of a simple one-dimensional model of longwave radiation transmission through a cloudy environment, following Stephens (1978). This permits simulations that include cloud-top radiational cooling effects, but no influence of gaseous absorption of longwave radiation, nor any shortwave interaction. Contributions to the turbulent kinetic energy may come from any or all of the following sources: surface heat flux, the existence of cloud-top instabilities, cloud-top radiational cooling, latent heat release, and wind shear.

This LES code is somewhat different than that of Moeng (1986). Moeng's code attempts to be more complete in its treatment of radiation, while the present code attempts a more complete treatment of subgrid partial cloudiness. With this enhanced subgrid partial cloudiness, we believe that our simulations have some validity even when the grid resolution is insufficient to ensure that the resolved-scale turbulence is much larger than the unresolved. This allows us, for the same computer resources, to investigate the effects of varying more input parameters. Because of this lack of a high degree of precision, we will not attempt detailed budget analysis of the turbulence statistics. The effective filtering of our model is incorporated into the subgrid model. We can increase the ratio of resolved turbulence to unresolved by reducing the scale, Λ_{max}, in the subgrid turbulence parameterization, as noted by Sykes and Henn (1989). If Λ_{max} is decreased too far, however, the apparent additional resolved turbulence is due more to grid-scale numerical noise than to the simulation of any real physical turbulence. Sensitivity of our results to changes in Λ_{max} are discussed in the appendix.

3. Simulation results

The different conditions for the matrix of runs discussed in this paper are shown in Tables 1 and 2. These runs are a representative sample from a larger matrix

TABLE 1. Physical input variables. The variable z_i is the inversion height, $\langle w'q_0' \rangle$ is the surface latent heat flux, $\langle w't_0' \rangle$ is the surface sensible heat flux, F_{Rd} is the downward radiation at the top of the boundary layer domain, du/dz is the vertical wind shear, and divergence is the large-scale divergence leading to subsidence in the domain.

Simulation number	z_i (m)	$\langle w'q_0' \rangle$ (W m^{-2})	$\langle w't_0' \rangle$ (W m^{-2})	F_{Rd} (W m^{-2})	du/dz 1 s^{-1}	divergence 1 s^{-1}
1	700	45	0	260	0	-5×10^{-6}
2	700	100	0	260	0	-5×10^{-6}
3	700	200	0	260	0	-5×10^{-6}
4	700	100	50	260	0	-5×10^{-6}
5	1200	0	100	160	0	-2.5×10^{-5}
6	1200	200	0	160	0	-2.5×10^{-5}
7	1200	200	0	160	4×10^{-3}	-2.5×10^{-5}
8	700	65	0	150	0	-5×10^{-6}
9	As in 1 but with different start-up.					
10	Restart of 2 with surface latent heat flux shut off.					
11–13, 16	As in 1.					
14, 15	As in 8.					
17	As in 5.					

TABLE 2. Numerical input variables.

Simulation number	Domain (km)	Grid points	Subgrid max scale (m)
1–4, 8–10	3 × 3 × 1.5	60 × 60 × 60	27.5
5–7	12 × 12 × 3	60 × 60 × 60	100
11	6 × 6 × 1.5	40 × 40 × 60	82.5
12	6 × 6 × 1.5	60 × 60 × 60	55
13	3 × 3 × 1.5	30 × 30 × 60	55
14	6 × 6 × 1.5	60 × 60 × 60	55
15	6 × 6 × 1.5	60 × 60 × 60	27.5
16	1D		200
17	1D		425

of simulations that was studied. Table 1 specifies the physical variables, while Table 2 lists the numerical inputs. A discussion of the sensitivity of the simulations to changes in the latter is deferred to the appendix. The simulations were initiated with some instability in the mean profiles and small random temperature fluctuations to encourage the development of resolved-scale motions. The details of the initial profile and perturbations were found to be unimportant, as each simulation was run for 3 hours, with only the last hour used for presenting the results (unless otherwise noted). The principal physical variables are sensible and latent surface heat fluxes, the downward radiation flux above the cloud, and the temperature, humidity, and velocity differences across the boundary layer. Reasonable values of subsidence were added to the simulations to make it easier to keep the cloud-top inversion in the region of fine vertical grid spacing. All of the simulations were run with modest wind speeds and a low surface roughness in order to keep the shear production of turbulent kinetic energy relatively low.

A set of large eddy simulations contains so much data that it is difficult to organize and present in an efficient manner. We will not attempt to present complete results, but rather try to selectively illuminate the influence of particular variables. Some of the 1-hour-averaged, characteristic statistical parameters from this matrix of runs are given in Table 3, and the statistical vertical profiles are shown in Figs. 1–3. These results will be discussed in turn as they relate to the effect of varying particular physical variables.

There is some inherent uncertainty in the results of any given simulation due to the random nature of the cloud turbulence. By choosing different random perturbations to start the simulation, we can obtain a different realization of the field variables for the same ensemble conditions chosen for the simulation. This is illustrated in Fig. 3 by comparing simulations S-1 and S-9, which differ only in how the start-up phase of the simulation was treated. The largest difference is approximately 10% in the maximum vertical velocity variance. These differences are a reflection of the fact that a 1-hour average over the turbulence in our relatively confined domain is not always adequate to provide a precise estimate of the ensemble average in these simulations where the timescale of an individual cloud can exceed 1/2 h. The observed sensitivity of the simulations to the variation of any physical input parameter is physically significant only to the extent that it exceeds this inherent level of uncertainty.

a. Buoyancy driven by latent versus sensible surface heat flux

When the boundary layer is in a stationary state with surface forcing, the Bowen ratio may be expected to be the appropriate parameter governing the impact of the vertical transport of water vapor on the structure of boundary layer clouds. Table 1 shows input values for simulations involving six different combinations of sensible and latent heat fluxes from the surface, encompassing three different values of the Bowen ratio. Figures 1 and 2 compare some average vertical profiles for these runs. For all cases these boundary layers are quasi-stationary with nearly linear profiles of heat and humidity flux as shown in Figs. 1e, 1f, 2e, and 2f. The heat flux shown is the sum of $\langle w'\theta_l' \rangle$ and Fr, the net radiation flux (shifted to be zero at the surface).

The surface Bowen ratio B is only a partial measure of the influence of latent heat release in the boundary layer. Even under stationary equilibrium conditions, the value of B does not set the ratio of fluxes in the cloud layer itself. If the turbulence is at least partially driven by cloud-top radiative or evaporative cooling, then the entrainment fluxes are also important sources of sensible and latent heat input. Also, in general, only a fraction of the latent heat available is actually released by phase change in boundary layer clouds. Perhaps a better measure of the influence of latent heat release than the Bowen ratio is the ratio of the buoyancy generated by any liquid water flux to the total buoyancy flux. As long as precipitation (which we are ignoring in this study) is negligible, this ratio should provide a direct measure of the impact of latent heat release on the turbulent dynamics, since the liquid water flux, $w'q_l'$, incorporates the total influence of change of phase on the buoyancy flux. We will define

$$\beta = \frac{\left(\frac{L\theta}{c_pT} - 1.61\theta_0\right)\int \langle w'q_l' \rangle dz}{\int \langle w'\theta_v' \rangle dz}, \qquad (1)$$

where the integral is taken vertically over the full height of the boundary layer, L is the latent heat of vaporization, c_p the specific heat, T the temperature, θ the potential temperature, and the subscript zero refers to a reference value. The coefficient comes from writing the buoyancy flux in terms of the sum of the fluxes of the

TABLE 3. Some output averages for hours 2–3. Here z_i is the inversion height, w^* the convective velocity defined in Eq. (2), PCF_{max} the maximum partial cloud fraction, q_{lmax} the maximum liquid water mixing ratio, CTEI the $c_p\delta\theta_l/(L\delta q)$, CTC the cloud-top cooling, β the measure of liquid water buoyancy flux as defined in Eq. (1), w_e the entrainment velocity, and sk_{max} the vertical velocity skewness at level with maximum w^3.

Simulation number	z_i (km)	w^* (m s^{-1})	q_{lmax} (g kg^{-1})	PCF_{max}	CTEI	CTC (W m^{-2})	β	w_e (cm s^{-1})	sk_{max}
1	0.8	0.71	0.153	0.88	0.65	48	1.23	0.96	0.2
2	0.82	0.77	0.137	0.77	0.6	42	1.73	1.34	1.26
3	0.86	0.93	0.115	0.55	0.54	39	2.17	2.24	1.7
4	0.82	1.02	0.097	0.57	0.53	28	0.29	1.35	0.93
5	1.74	1.83	0.15	0.48	0.69	110	0.5	4.34	0.73
6	1.75	1.46	0.212	0.49	0.71	117	2.23	5.14	0.95
7	1.71	1.41	0.168	0.41	0.67	100	2.22	5.79	0.62
8	0.93	1.13	0.269	0.94	0.8	178	0.76	1.98	−0.73
9	0.8	0.7	0.16	0.85	0.63	48	1.53	1.31	0.55
10	0.84	0.46	0.107	0.94	0.68	35	0.8	0.12	−0.47
11	0.81	0.65	0.171	0.95	0.67	55	1.12	0.68	−0.08
12	0.79	0.7	0.159	0.86	0.63	48	1.48	1.23	0.45
13	0.79	0.69	0.152	0.85	0.64	47	1.45	1.23	0.43
14	0.94	1.06	0.252	0.8	0.81	174	0.88	2.48	−0.55
15	0.92	1.12	0.254	0.93	0.79	175	0.76	2.44	−0.66
16	0.8	0.74	0.207	0.92	0.69	68	0.89	0.96	0
17	1.69	1.98	0.191	0.73	0.65	170	0.25	4.22	0

two conserved variables, liquid potential temperature and total water mixing ratio, and the liquid water flux [Eq. (24) of Lewellen and Yoh 1993]. The resulting coefficient of the liquid water flux is the expression given in parenthesis. The first term represents the heat released by condensation and the second, negative term the influence of the increased density due to the liquid drops.

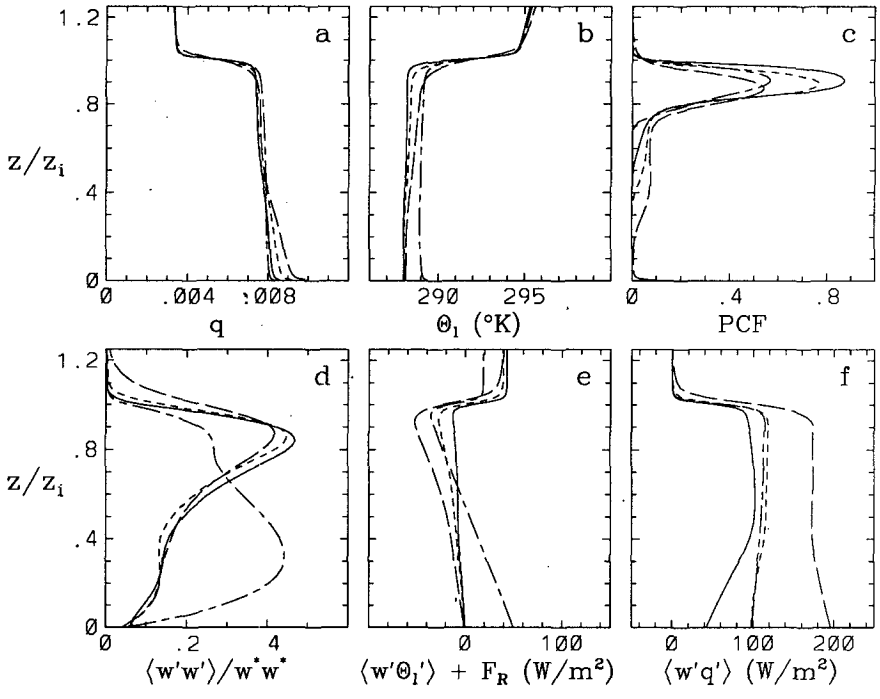

FIG. 1. Hour-averaged statistics as a function of height for some simulations that demonstrate the effect of varying the surface Bowen ratio in a relatively shallow boundary layer (solid line, S-1; short dashes, S-2; long dashes, S-3; short and long dashes, S-4). (a) Total water mixing ratio, (b) liquid potential temperature, (c) partial cloud fraction, (d) vertical velocity variance, (e) heat flux (sensible plus radiation), and (f) total water flux.

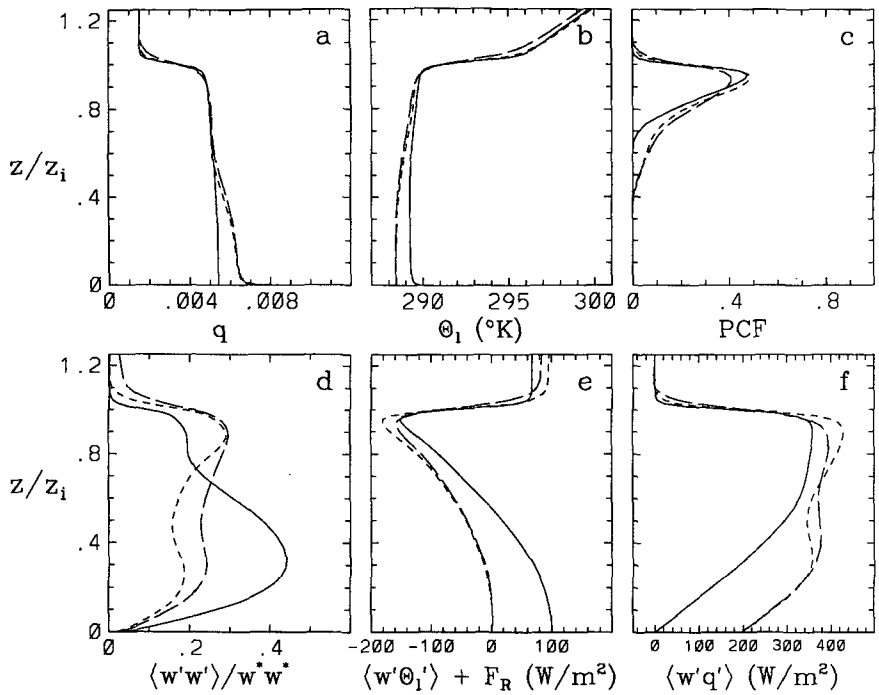

FIG. 2. Hour-averaged statistics as a function of height for some simulations that demonstrate the effect of varying the surface Bowen ratio and wind shear in a relatively deep boundary layer (solid line, S-5; short dashes, S-6; long dashes, S-7). (a) Total water mixing ratio, (b) liquid potential temperature, (c) partial cloud fraction, (d) vertical velocity variance, (e) heat flux (sensible plus radiation), and (f) total water flux.

It should be noted that the value of β is not confined between 0 and 1. It may be negative but seldom is, since this would require there to be more liquid water in regions of negative w than in regions of positive w. But it can readily exceed one, since part of the buoyancy generated by the liquid water flux is often canceled by a negative sensible heat flux. The value of β for the different simulations is given in Table 3. The simulations in which the surface latent heat flux dominates the dynamics all have a value of β well over 1. As seen in Table 3, however, it is possible to have $\beta > 0.5$ with quite different dynamics (e.g., simulation 8 is largely driven by cloud-top radiational and evaporative cooling, as will be discussed in the next section).

The results summarized in Figs. 1 and 2 and Table 3 show three prominent differences between boundary layers whose dynamics are dominated by latent versus sensible heat flux from the surface. First, for the same surface heating, the sensible heat transfer is much more efficient in generating buoyantly driven turbulence. Comparison of the values of w^*, defined here as

$$w^* = \left[2\,(g/\theta_0) \int \langle w'\theta_v' \rangle dz \right]^{1/3}, \qquad (2)$$

show, for example, that simulation S-5, driven by surface sensible heat flux, produces more buoyant energy than S-6, with twice the surface heat flux but in the form of latent heat. Similarly, simulation S-4 is dominated by the surface sensible heat flux even though the surface latent heat flux is twice as large. Second, as the importance of the surface latent heat flux increases, there is a lower tail on the cloud fraction profile (Figs. 1c, 2c). In simulation S-3, for example, increasing the surface latent heat flux to 200 W m^{-2} lowers the cloud ceiling in the updrafts to $\sim 1/4$ of the mixed-layer height. Since we can expect the water vapor to be essentially carried by the large eddies over the central portion of the boundary layer, the updrafts may be expected to have a lower condensation level than that of the downdrafts when the latent heat flux is much larger than the sensible heat flux; that is, $B \ll 1$. Finally, there is a tendency for the boundary layer to be less well mixed when the dynamics are dominated by the latent heat flux from the surface. This may be seen in both the humidity and temperature profiles, Figs. 1a, 1b, 2a, and 2b.

The dominance of sensible over latent heat flux at the surface arises simply because not all of the latent heat introduced at the surface gets converted into buoyancy and most of the conversion occurs in the upper regions of the boundary layer where it has less available height to release potential energy. A corollary to this is that updrafts driven by latent heat release tend to be fewer and stronger than those driven by surface sensi-

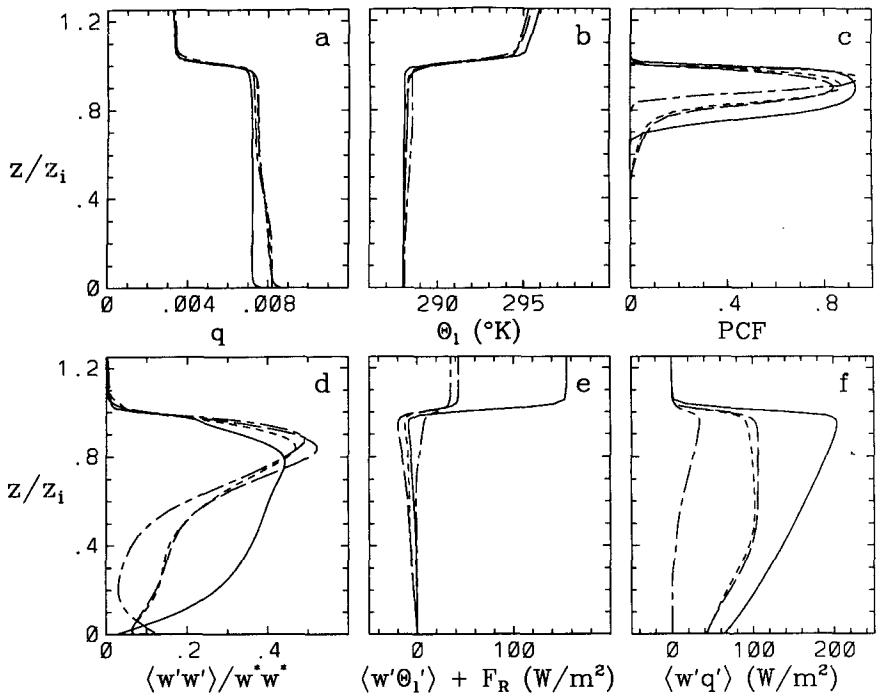

FIG. 3. Hour-averaged statistics as a function of height for some simulations that demonstrate the effect of varying cloud-top cooling, different start-up, and decoupling (solid line, S-8; short dashes, S-1; long dashes, S-9; short and long dashes, S-10). (a) Total water mixing ratio, (b) liquid potential temperature, (c) partial cloud fraction, (d) vertical velocity variance, (e) heat flux (sensible plus radiation), and (f) total water flux.

ble heat flux, since only a few purely moisture-driven updrafts are strong enough to rise above the lifting condensation level and thereby generate appreciable buoyancy to sustain themselves. As a result, the moisture is essentially carried across the middle of the boundary layer by the updrafts, which, accordingly, have a substantially lower condensation level than the downdrafts. This gives rise to the lower tail in the vertical cloud fraction profile. This correlation of column clouds with strong updrafts was confirmed directly by examining 3D velocity and liquid water fields from our simulations. Outside of the cloudy updrafts, the dryer, subsiding air tends to stabilize the boundary layer and result in less well mixed humidity and temperature profiles as seen in Figs. 1a, 1b, 2a, and 2b. When $\beta > 1$, part of the buoyancy generated by the liquid water flux drives a negative sensible heat flux, yielding a slightly stable lapse rate in the middle of the boundary layer. However, adding any appreciable low-level turbulence, whether by including significant surface sensible heat flux (raising the Bowen ratio) as in simulation S-4 or by penetrating downdrafts resulting from cloud-top cooling as in S-8, remixes the boundary layer and eliminates these features.

When $\beta > 1$, the tendency toward conditionally stable lapse rates (i.e., potential temperature gradients that would be stable in the absence of any water change of phase) provides the potential for subsequent decoupling between the cloud and subcloud portion of the boundary layer. This is illustrated by simulations S-2 and S-10, which both show a small but distinct stable gradient in θ_l within the conventional "mixed boundary layer" (Fig. 3). Simulation S-10 is a continuation of S-2 with the surface humidity flux shut off. There is no major difference in the temperature or humidity profiles, but the humidity flux profile shows that there is no humidity flux below cloud level. The boundary layer now has partial decoupling with a distinct local minimum in vertical velocity variance near cloud base, as seen in Fig. 3d. The potential for decoupling was established in S-2, with its large value of β, and realized in the subsequent S-10 when the surface humidity flux was shut off.

The lower tail on the cloud fraction profiles in the low Bowen ratio simulations can be presented in a different format, as a cloud ceiling frequency, for purposes of comparing with some field data. The ASTEX data summary by Cox et al. (1993) shows frequencies of ceiling heights as measured by lidar. They use the lidar pointed straight up and measure the height of the cloud bottom every minute. Then using 50-m interval bins, they plot frequency versus height (number in interval versus height in km) for each day. Heights > 3 km are recorded but not shown on the plot. We obtain

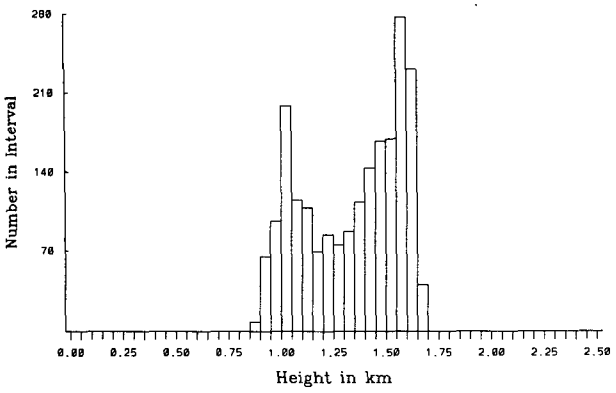

FIG. 4. Cloud structure as exhibited by viewing the histogram of ceiling frequency for simulation 7.

a comparable plot by integrating the liquid water upward and recording the height at which a threshold depth is reached at each grid point for a given simulation time. Figure 4 shows the result for simulation S-7 at 2.5 h with an integrated liquid water threshold of 6 gm m^{-2}. Fig. 5 shows a representative day from the data. This is only a qualitative comparison (there is, for example, some dependence on the value of integrated liquid water used to locate the cloud base), but our curves for the lower values of B show the same type of bimodal distribution about two cloud heights, with the lower heights corresponding to the condensation level for the updrafts.

To illustrate that the lower-cloud ceilings are indeed associated with the updrafts, we computed the fraction of the liquid water in the updrafts for 1 km $< z <$ 1.25 km, which is the region between the lower maximum and the local minimum above it in Fig. 4. Approximately 75% of the liquid water at this level is in updrafts with vertical velocity > 0.5 m s^{-1}. The corresponding cross-sectional area of these updrafts is only one-sixth of the horizontal domain.

b. *Cloud-top radiational cooling*

Cloud-top radiational cooling has a major impact on the dynamics of the cloudy boundary layer. It provides an energy sink that tends to promote condensation and increase cloudiness. Since this energy sink occurs at the top of the boundary layer, it is also a direct source of buoyancy and, thus, can significantly increase the turbulent kinetic energy (TKE). In the simulations considered here, the downward longwave radiation flux above the cloud is held constant with time in each case. This is not the same as holding the cloud-top cooling constant. There is a positive feedback between the radiational cooling and the liquid water condensation; thus, the simulations producing stronger cooling at cloud top tend to be those that have larger liquid water content in the cloud layer and vice versa.

Simulations S-1 and S-8 differ only by the specification of the downward radiation flux (the modest difference in surface latent heat flux listed in Table 1 is also a consequence of this difference in radiation flux, since the surface humidity was held fixed at the same value in both these runs). In the simulation with the smaller downward longwave radiation flux, larger radiational cooling yields a maximum liquid water content 1.76 times that for S-1 (Table 3), although this leads to only a modest difference in liquid potential temperature in the top of the cloud as seen in Fig. 3b. Table 3 also shows that w^{*2} is increased by 2.53 and that the entrainment velocity is increased by a factor of 2.06. Thus, the additional cooling results in slightly reduced θ_l, increased liquid water, increased TKE, and increased potential energy via increased entrainment. Since $\beta = 0.76$, the flow is driven primarily by the liquid water flux. This together with the negative vertical velocity skewness, which indicates narrow downdrafts are more active than updrafts for this case, suggest that the downdrafts are driven more by evaporative cooling than by direct radiational cooling.

Figure 6 exhibits the striking difference between the cloud structure observed for S-8 and S-3 by showing the vertically integrated liquid water content at a typical time within the two simulations. Simulation S-3, which is dominated by the surface latent heat flux, shows a number of puffy structures induced by fairly concentrated buoyant plumes, while the S-8 structure exhibits quite narrow ribbons of fairly clear downdrafts. These structural differences are also directly reflected by the contrast in skewness in the vertical velocity fluctuations given in Table 3. In both cases the turbulent eddies are driven mainly by the buoyancy generated from a positive liquid water flux, as indicated by the values of β in Table 3. The strongest driving mechanism appears to be condensation within the updrafts in one case and evaporation in the downdrafts in the other.

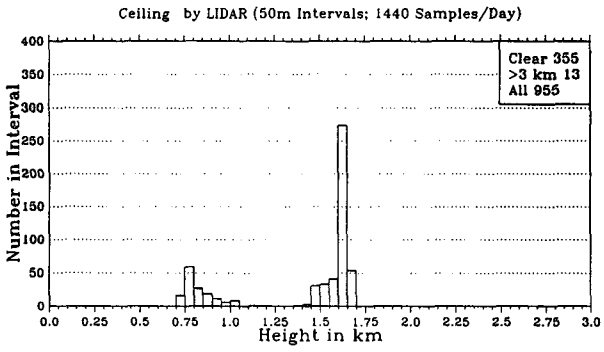

FIG. 5. Histogram of cloud ceiling frequency observed during ASTEX observations at Porto Santo in the Madeira Islands on 25 June 1992 (Cox et al. 1993).

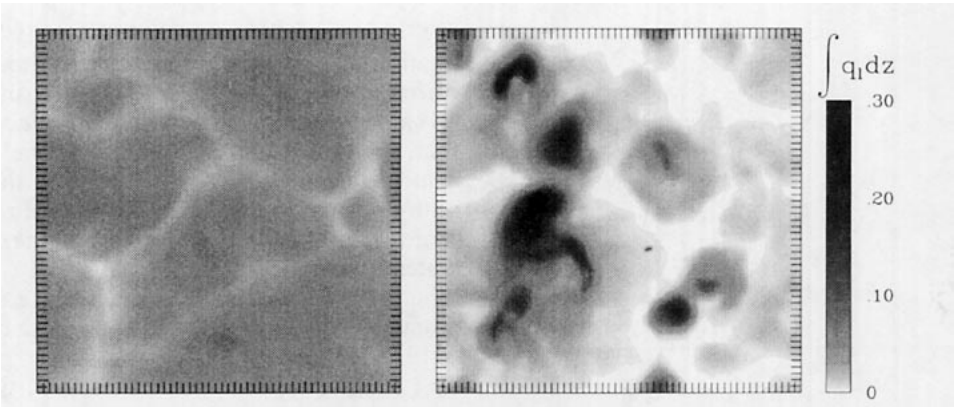

FIG. 6. Contrast between the cloud structure resulting from top-driven vs surface-driven buoyancy as exhibited by viewing the vertically integrated liquid water content for (a) S-8 and (b) S-3.

c. *Cloud-top entrainment instability*

The ratio of the temperature jump to the humidity jump at the top of the cloud layer determines whether the entrainment of environmental air into the cloud layer induces an evaporation instability in the top of the cloud (Lilly 1968; Deardorff 1980; Randall 1980). This cloud-top entrainment/instability ratio, CTEI, taken here as $c_p\delta\theta_l/(L\delta q)$, is an input parameter, which then may change with time as the boundary layer grows. We include its average value over the last hour as an output variable in Table 3. Several analyses (e.g., Tag and Payne 1987; Kuo and Schubert 1988; Albrecht 1991; MacVean 1993) have been aimed at determining how low CTEI must be for the cloud layer to break up. It has previously been established that small-scale mixing induced by an unstable CTEI can partially release the instability (MacVean and Mason 1990; Lewellen and Yoh 1993), leading to a different value of CTEI for larger-scale instability. This small-scale partial cloud influence on CTEI is included as part of our subgrid partial cloudiness formulation.

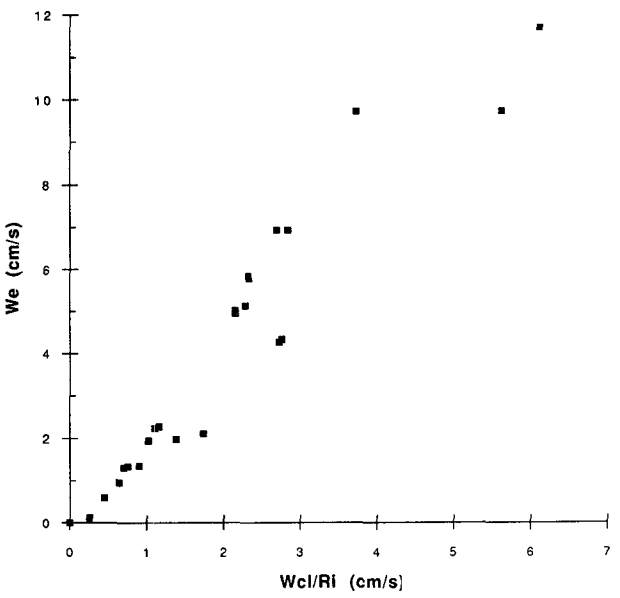

FIG. 7. Cloud-top entrainment as a function of the appropriate Richardson number defined in Eq. (3).

Cloud-top entrainment instability is expected to have a strong impact on the entrainment velocity, but such effects may be compensated by resulting changes in the partial cloud fraction. We find that the entrainment velocity correlates quite well with a Richardson number Ri based on the buoyancy jump across the inversion ($\delta\theta_v$), the vertical velocity variance at the height of maximum PCF, (w_{cl}^2), and a length scale based on the cloud-top thickness as measured by the difference between the height of the maximum cloud fraction and the height of the steepest gradient in total humidity (z_{c-t}), that is,

$$w_e = \frac{w_{cl}}{\mathrm{Ri}}; \quad \text{with} \quad \mathrm{Ri} = \left(\frac{g}{\theta_0}\right)\left(\delta\theta_v \frac{z_{c-t}}{w_{cl}^2}\right). \quad (3)$$

This is demonstrated in Fig. 7. This correlation implies that the gain in potential energy due to the rise in the inversion height is essentially a constant fraction of the turbulent kinetic energy within the cloud layer. There is some scatter in Fig. 7 but relatively little given the major differences in the mechanisms for generating the buoyancy within these runs. We have included runs where the buoyancy is generated by surface sensible heat flux, latent heat flux, cloud-top radiational cooling, and cloud-top entrainment instability. For Fig. 7, as well as Figs. 8 and 9 below, we have included results of some additional simulations not listed in Tables 1–3, including some alternate realizations and different combinations of wind shear and surface fluxes. We have not studied how this correlation might be changed if the turbulence is dominated by wind shear at cloud top.

Our results show some correlation between CTEI and partial cloud fraction (PCF), but there is considerable scatter. Lewellen and Yoh (1993) predicted that the relation between CTEI and PCF should be highly dependent on

the vertical velocity skewness in the cloud layer, so the scatter is not unexpected. They also asserted that there should be a much weaker impact of skewness on PCF when PCF is considered as a function of the Sommeria and Deardorff (1977) relation derived from the Gaussian probability distribution. Figure 8 shows a very good correlation between PCF and the cloud fraction,

$$\bar{r} = \frac{1}{2} - \frac{1}{2}\,\mathrm{erf}(\zeta/(2)^{1/2}), \qquad (4)$$

predicted by the Gaussian relations. The variable ζ in Eq. (4) is the ratio of the mean saturation excess to the square root of the saturation variance. This strong correlation indicates that the variation of skewness in the simulations shown here has no discernable impact on this correlation. Of course, this is a relationship that can only be utilized within a model if information on the saturation variance is included; however, Fig. 9 shows that there is a nearly useable correlation between the PCF and the relative total humidity at the level of maximum PCF so that a precise prediction of the saturation variance should not be required.

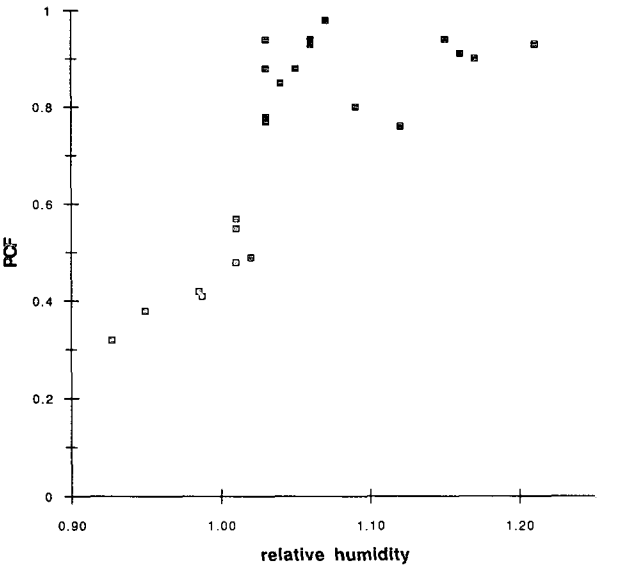

FIG. 9. Maximum partial cloud fraction as a function of relative humidity at that level.

d. Wind shear in the boundary layer

The differences shown in the vertical profiles for S-6 and S-7 (Fig. 2), due to a variation in wind shear across the boundary layer, are quite modest. These small differences cannot be considered physically significant given the differences observed between two random realizations (e.g., the differences between S-1 and S-9). Shear seems to have two competing effects on the turbulence in the boundary layer. It provides for some direct conversion of mean flow energy into turbulent energy, but it also appears to have a slight dampening effect on the buoyant plumes, so the net effect may be either an increase or decrease in the level of total turbulence in the cloudy boundary layer.

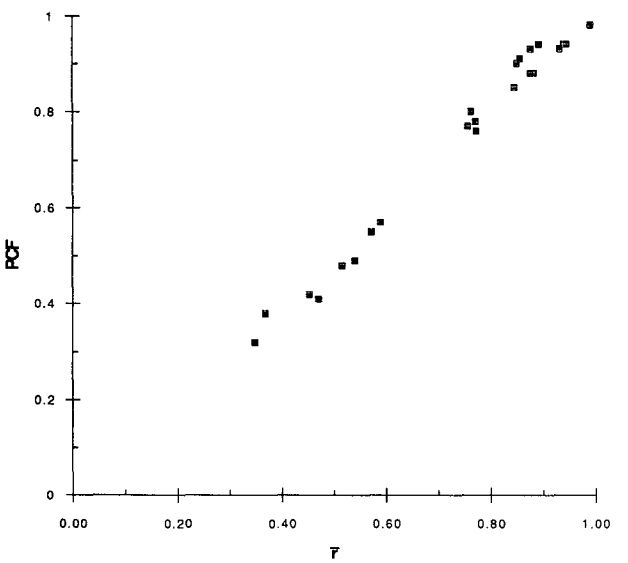

FIG. 8. Maximum partial cloud fraction compared with the $\bar{r}$ function of the ratio of mean saturation difference from 1 to the square root of the saturation variance derived by Sommeria and Deardorff (1977) and given in Eq. (4).

The major effect of shear in our model runs is in the coherent organization of the clouds. The effects of shear in organizing flows in dry convection are well documented. Sykes and Henn (1989), for example, showed that the ratio of surface shear to buoyancy determines the generation of convective rolls in the boundary layer. They concluded that rolls occur for $u^*/w^* > 0.35$. Moeng and Sullivan (1994) found a higher value of 0.65 required for the onset of rolls in their simulations. In our simulations, u^*/w^* is lower than 0.3 and, thus, by this criterion should not yield this type of cloud street organization; however, the previous dry simulations do not address the requirements for roll alignment when the buoyancy is supplied by latent heat release. In the simulations reported here, we did not generally observe a roll-type organization of the clouds, except for short intervals during the start-up of some of the runs. The addition of geostrophic shear, however, did allow the boundary layer cloud circulations to become more organized. There are somewhat fewer buoyant plumes penetrating through the boundary layer, and the individual plumes are more clustered. This allows a few coherent clusters to present a persistent cloud circulation. This organizing effect of the wind shear was found to be more pronounced in the presence of a low Bowen ratio.

In the initial part of our simulations including wind shear (illustrated here by simulation S-7), the wind

shear organizes the cloud structure into streets as expected. As simulation time proceeds, the cloud street spacing grows, both as a result of the boundary layer growth and as a result of the merging of the rolls. The two-dimensional simulations of Sykes et al. (1988) demonstrated that the ratio of cloud street spacing to boundary-layer thickness tends to be increased in the presence of appreciable cloud-top entrainment. Their simulations showed that this cloud street aspect ratio could be increased to values greater than 10. Our current 3D LESs show that there is also a clumping of the principal updrafts in an individual cloud street. Within 2 h of simulated time, these combined processes of street merging and the clumping of individual streets can lead to a persistent cluster of updrafts in our 12-km domain. At this stage, the single microscale circulation system can persist for more than an hour.

Figure 10 illustrates the coherency introduced by a modest shear and low Bowen ratio. The vertically integrated liquid water is shown as a function of x and y at the 2.5-h point of two simulations that differ by their Bowen ratio and wind shear. Figure 10a is from S-7 with $B \sim 0$ and a modest wind shear, while 10b is from S-5 with a large Bowen ratio and no geostrophic shear. Figure 10b shows a quite random distribution of clouds tied to the same distribution of updrafts, but Fig. 10a shows that the updrafts and corresponding clouds are no longer randomly distributed. They are clustered, with the lifetime of the cluster observed to be significantly longer than the lifetime of the individual updrafts, exceeding 1 h in some simulations such as this one.

4. Conclusions

Some conclusions that follow from an examination of these LES results are as follows. A low Bowen ratio boundary layer tends to produce a cloud layer with a highly bimodal character to the cloud ceiling frequency. The updrafts produce a lower cloud ceiling than the surrounding environment with weak downdrafts.

When the surface latent heat flux plays the dominant role in the dynamics of the turbulence in the boundary layer, a slight positive gradient in θ_l develops that favors the potential for subsequent decoupling to occur near the lifting condensation level.

A very low Bowen ratio with the aid of some boundary layer shear makes the development of persistent microcell cloud circulations possible within the boundary layer. A large difference in relative humidity between parcels of air in the updrafts and that in the downdrafts leads to condensation levels at much lower altitudes in the updrafts. This allows the updrafts to show up visibly as clouds. The addition of moderate shear favors the organization of these column clouds into a few, relatively long-lived cells. Such cells were observed in the ASTEX field experiment.

The hour-averaged, maximum partial cloud fraction is very well represented by the relation derived by Sommeria and Deardorff (1977) for saturation fluctuations with a Gaussian probability distribution function. The maximum partial cloud fraction also appears to be roughly correlated with relative humidity at the level of maximum partial cloud fraction.

The entrainment velocity of the cloud-top inversion is proportional to the square root of the vertical velocity variance at the maximum PCF level (w_{cl}) divided by a Richardson number based on the virtual potential temperature jump across the cloud top, the thickness of the cloud top, and w_{cl}^2, regardless of the mechanism responsible for generating the buoyancy.

Acknowledgments. This work was supported by a grant from the Office of Naval Research with R. F. Abbey Jr., technical monitor.

APPENDIX

Numerical Sensitivity

The primary numerical parameters in our simulations are the grid resolution, the subgrid turbulence scale Λ,

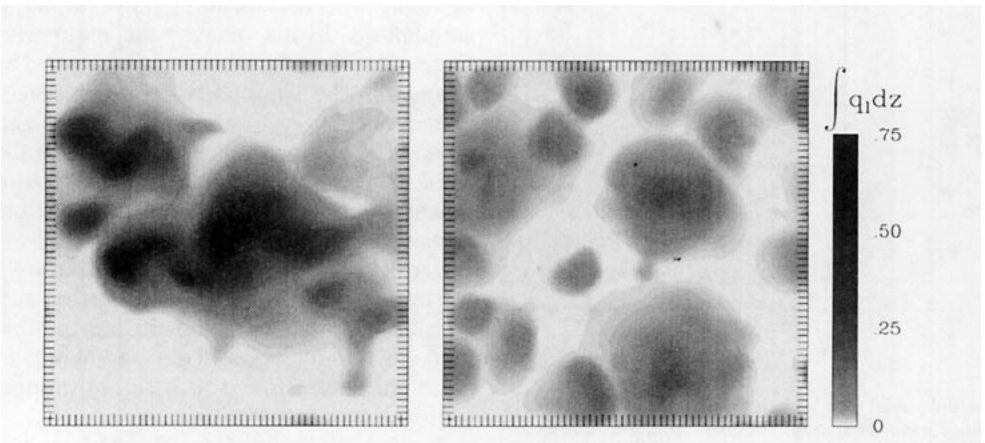

FIG. 10. Effect of modest wind shear on cloud structure as exhibited by viewing the vertically integrated liquid water content for (a) S-7 and (b) S-5.

and the domain size. We sketch the sensitivity of the simulations to changes in these parameters below. In varying the first two, the intent is to show how the nature of the simulation changes as the division between resolved and unresolved turbulence changes. By incorporating valid subgrid parameterization, it should be possible to allow more of the energy to remain unresolved and still keep the simulation reasonable for many of the variables. We use a stretched vertical grid with relatively fine spacing near the surface and in the neighborhood of the inversion, since these are the boundaries where our "large eddies" are undergoing the sharpest changes. How much of the turbulent kinetic energy can be resolved is then largely determined by the horizontal resolution, which is a compromise between domain size and number of grid points.

a. Grid resolution

A comparison in Fig. A1 between the results of S-9 and S-13 allows the impact of a 50% decrease in the number of horizontal grid points in each direction in the same domain to be investigated. There is noticeable variation in the resulting total statistics, but this variation appears to be within that attributable to different random realizations and, thus, cannot be deemed statistically significant. There is a modest but significant difference in the fraction of the total turbulence, which is in the resolved scale. We believe this is primarily because the subgrid scale, Λ, has been increased as the horizontal grid length was increased. This effect is isolated in the next section. When the grid resolution is coarsened yet further, as in S-11, the differences become more pronounced.

With the present subgrid parameterization it is possible to go smoothly over to the limit of no resolved turbulence. In such a 1D limit, all of the turbulence is unresolved. Comparisons in Fig. A2 between the 1D simulation of S-16 and the standard resolution S-1 in fact show that the average statistics are rather similar. The largest difference is in the turbulent kinetic energy in the top part of the boundary layer, where the 1D simulation cannot pick up the large horizontal velocities. Note that even the partial cloud fraction profiles are similar. In the resolved case the dominant cloud cells are resolved, and the partial cloud fraction is resolved, while in the 1D case this information must be carried by the subgrid parameterization. This is consistent with Fig. 7, which showed that in all of these runs the resolved PCF is similar to the function used for the subgrid parameterization. The relative success of the 1D simulation in this case lends strong support to the validity of the subgrid parameterization for the LES. However, the possibility that the subgrid relationship

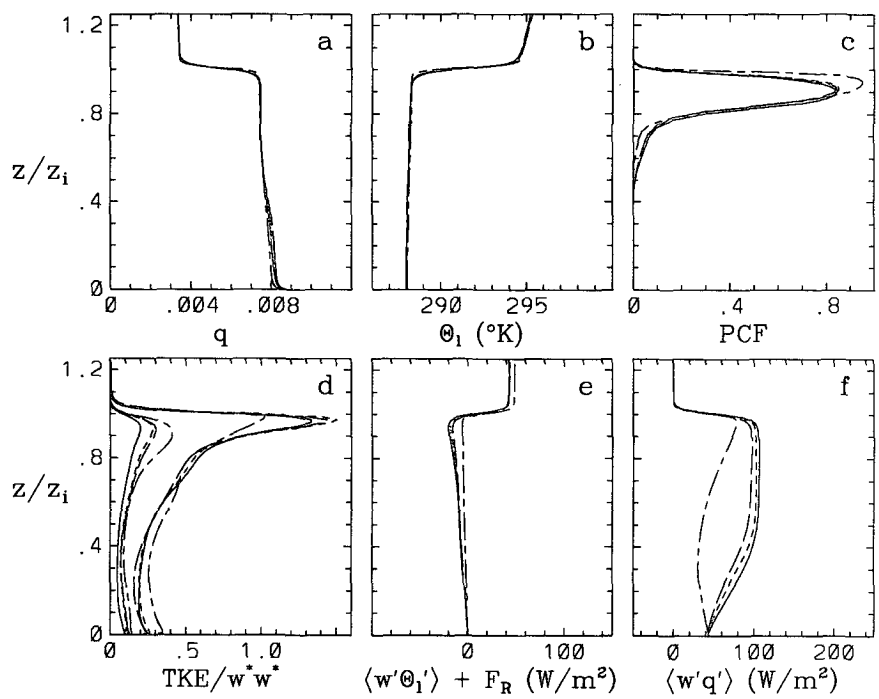

FIG. A1. Hour-averaged statistics as a function of height for some simulations that demonstrate the effect of varying resolution and domain size (solid line, S-9; short dashes, S-12; long dashes, S-13; short and long dashes, S-11). (a) Total water mixing ratio; (b) liquid potential temperature, (c) partial cloud fraction, (d) turbulent kinetic energy both total and subgrid, (e) heat flux (sensible plus radiation), and (f) total water flux.

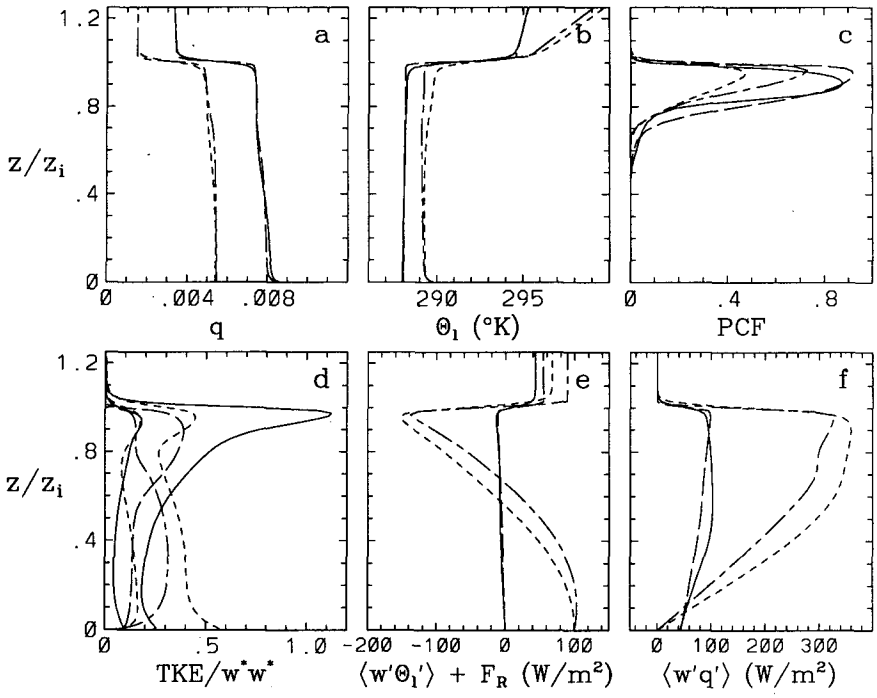

FIG. A2. Comparison between the hour-averaged statistics as a function of height for the completely unresolved, 1D simulations and the LES results for standard resolution (solid line, S-1; short dashes, S-5; long dashes, S-16; short and long dashes, S-17). (a) Total water mixing ratio, (b) liquid potential temperature, (c) partial cloud fraction, (d) turbulent kinetic energy both total and subgrid, (e) heat flux (sensible plus radiation), and (f) total water flux.

is having an undue influence, even when the PCF is primarily resolved, is difficult to completely rule out. Further, the production of small-scale energy close to cloud top means that less of this production is resolved even in the high-resolution runs. Thus, there is some uncertainty as to how reliable the entrainment results are in these cases.

It should be noted that the PCF is not as well simulated by the 1D model for simulation 5, which has the buoyancy dominated by surface sensible heat flux, as noted by comparing S-17 with S-5 in the same figure. Both the heat and moisture fluxes are quite similar, but the 1D model does not permit the slight counter gradient flux observed in the resolved simulation. The consequent differences in humidity and temperature are not very large in the mean profiles in (a) and (b), but they help contribute to the quite significant difference seen in PCF in (c). The vertical transport of the turbulence is more important in the sensible heat case with most of the turbulent kinetic energy produced lower in the boundary layer.

b. Subgrid-scale size

As noted in the review of the model, we can increase the ratio of resolved turbulence to unresolved turbulence by reducing the scale, Λ_{max}, of the subgrid turbulent parameterization (Sykes and Henn 1989). However, if Λ_{max} is decreased too far, a significant fraction of the additional apparent resolved turbulence is due to grid-scale numerical noise rather than to the simulation of any real physical turbulence. Thus, there is a minimum Λ_{max} for a valid simulation for any given grid size. Our standard value of Λ_{max} for the simulations presented in this work is half of the horizontal grid spacing, which we believe is well above this minimum limit. A comparison between the results of simulations S-8, S-14, and S-15 in Fig. A3 illustrates that we can further reduce Λ_{max} to one-quarter of the horizontal grid spacing without adding any spurious noise component to the turbulent kinetic energy. Indeed, for the physical conditions of these runs (in which the dominant circulations are relatively thin walls or cracks of downdrafts driven by cloud-top cooling, cf. Fig. 6a), the lower value of Λ_{max} results in the better simulation for the coarser resolutions in S-14 and S-15, by permitting smaller-scale structures to be resolved.

c. Domain size

The simulations shown in this paper were computed on horizontal domains varying from 3 km × 3 km to 12 km × 12 km. The smallest domain was used for shallow boundary layers where cloud scales of a few hundred

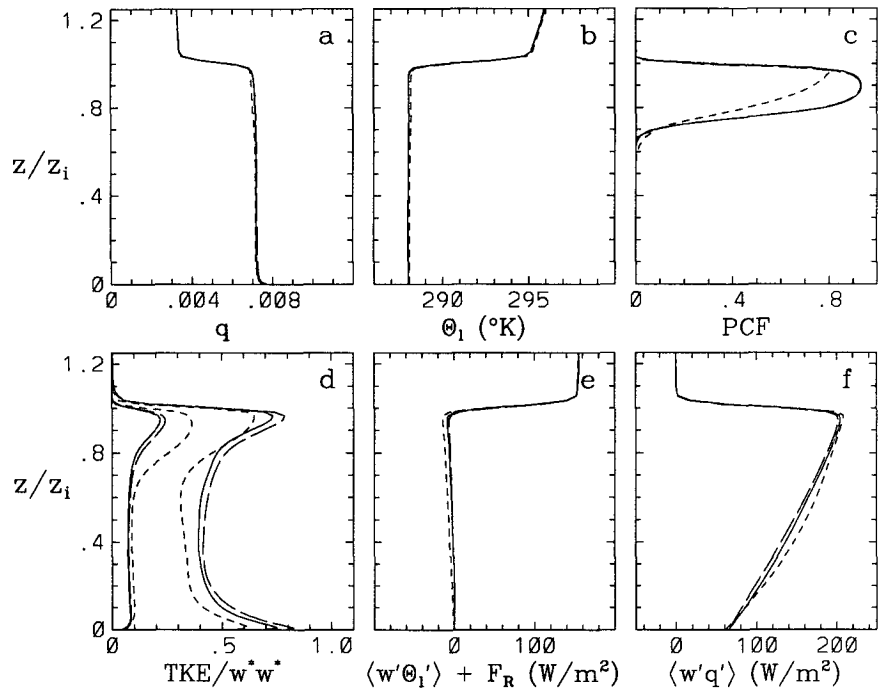

FIG. A3. Hour-averaged statistics as a function of height for some simulations that demonstrate the effect of varying subgrid turbulent length scale (solid line, S-8; short dashes, S-14; long dashes, S-15). (a) Total water mixing ratio, (b) liquid potential temperature, (c) partial cloud fraction, (d) turbulent kinetic energy both total and subgrid, (e) heat flux (sensible plus radiation), and (f) total water flux.

meters were found. In the deep boundary layer, where cloud scales of the order of 1 km were anticipated, the large domain of 12 km × 12 km allows freedom for several cloudy plumes to be present at any one time. This allows a single interacting cloud system to dominate a larger area, as it appears to do in simulation S-7.

A comparison between the results of S-12 and S-13 in Fig. A1 allows the impact of the change in the domain to be isolated. There is almost no difference in the average profiles, but the increased domain size does allow the clouds to become organized on a slightly larger coherent scale.

REFERENCES

Albrecht, B. A., 1991: Fractional cloudiness and cloud-top entrainment instability. *J. Atmos. Sci.*, **48,** 1519–1525.

Cotton, W. R., and R. A. Anthes, 1989: *Storm and Cloud Dynamics.* Academic Press, 872 pp.

Cox, S., S. Gilles, A. Heidinger, and C. Keith, 1993: CSU ASTEX surface data sets from Porto Santo (June 1–28, 1992). Department of Atmospheric Science Paper 530, 155 p. [Available from Dept. of Atmospheric Science, Colorado State University, Boulder, CO 80523.]

Deardorff, J. W., 1980: Cloud top entrainment instability. *J. Atmos. Sci.*, **37,** 131–147.

Emanuel, K. A., 1994: *Atmospheric Convection.* Oxford University Press, 580 pp.

Kuo, H.-C., and W. H. Schubert, 1988: Stability of cloud-topped boundary layers. *Quart. J. Roy. Meteor. Soc.*, **114,** 887–916.

Lewellen, W. S., and S. Yoh, 1993: Binormal model of ensemble partial cloudiness. *J. Atmos. Sci.*, **50,** 1228–1237.

Lilly, D. K., 1968: Models of cloud-topped mixed layers under a strong inversion. *Quart. J. Roy. Meteor. Soc.*, **94,** 292–309.

MacVean, M. K., 1993: A numerical investigation of the criterion for cloud-top entrainment instability. *J. Atmos. Sci.*, **50,** 2481–2495.

——, and P. J. Mason, 1990: Cloud-top entrainment instability through small-scale mixing and its parameterization in numerical models. *J. Atmos. Sci.*, **47,** 1012–1030.

Mellor, G. L., 1977: The Guassian cloud model relations. *J. Atmos. Sci.*, **34,** 356–358; Corrigendum, **34,** 1483–1484.

Moeng, C. H., 1986: Large-eddy simulations of a stratus-topped boundary. Part I: Structure and budgets. *J. Atmos. Sci.*, **43,** 2886–2900.

——, and P. P. Sullivan, 1994: A comparison of shear- and buoyancy-driven planetary boundary layer flows. *J. Atmos. Sci.*, **51,** 999–1022.

——, S. Shen, and D. A. Randall, 1992: Physical processes within the nocturnal stratus-topped boundary layer. *J. Atmos. Sci.*, **49,** 2384–2401.

Randall, D. A., 1980: Conditional instability of the first kind upside-down. *J. Atmos. Sci.*, **37,** 125–130.

Sommeria, G., and J. W. Deardorff, 1977: Subgrid-scale condensation in models of nonprecipitating clouds. *J. Atmos. Sci.*, **34,** 344–355.

Stephens, G. L., 1978: Radiational profiles in extended water clouds. II: Parameterization schemes. *J. Atmos. Sci.*, **35,** 2123–2132.

Sykes, R. I., and D. S. Henn, 1989: Large-eddy simulation of turbulent sheared convection. *J. Atmos. Sci.*, **46,** 1106–1118.

——, W. S. Lewellen, and D. S. Henn, 1990: Numerical simulation of the boundary layer eddy structure during the cold-air outbreak of GALE IOP-2. *Mon. Wea. Rev.*, **118,** 363–374.

——, S. F. Parker, D. S. Henn, and W. S. Lewellen, 1994: Turbulent mixing with chemical reaction in the planetary boundary layer. *J. Appl. Meteor.*, **33,** 825–834.

Tag, P. M., and S. W. Payne, 1987: An examination of the breakup of marine stratus: A three-dimensional numerical investigation. *J. Atmos. Sci.*, **44,** 208–223.